Commun. Comput. Phys.
doi: 10.4208/cicp.150115.210715s

Vol. **18**, No. 4, pp. 1122-1146
October 2015

Dynamics and Instability of a Vortex Ring Impinging on a Wall

Heng Ren and Xi-Yun Lu*

Department of Modern Mechanics, University of Science and Technology of China, Hefei, Anhui 230026, China.

Received 15 January 2015; Accepted (in revised version) 21 July 2015

Abstract. Dynamics and instability of a vortex ring impinging on a wall were investigated by means of large eddy simulation for two vortex core thicknesses corresponding to thin and thick vortex rings. Various fundamental mechanisms dictating the flow behaviors, such as evolution of vortical structures, formation of vortices wrapping around vortex rings, instability and breakdown of vortex rings, and transition from laminar to turbulent state, have been studied systematically. The evolution of vortical structures is elucidated and the formation of the loop-like and hair-pin vortices wrapping around the vortex rings (called briefly wrapping vortices) is clarified. Analysis of the enstrophy of wrapping vortices and turbulent kinetic energy (TKE) in flow field indicates that the formation and evolution of wrapping vortices are closely associated with the flow transition to turbulent state. It is found that the temporal development of wrapping vortices and the growth rate of axial flow generated around the circumference of the core region for the thin ring are faster than those for the thick ring. The azimuthal instabilities of primary and secondary vortex rings are analyzed and the development of modal energies is investigated to reveal the flow transition to turbulent state. The modal energy decay follows a characteristic $-5/3$ power law, indicating that the vortical flow has become turbulence. Moreover, it is identified that the TKE with a major contribution of the azimuthal component is mainly distributed in the core region of vortex rings. The results obtained in this study provide physical insight of the mechanisms relevant to the vortical flow evolution from laminar to turbulent state.

AMS subject classifications: 76F65, 76D17, 76F06

Key words: Large eddy simulation, vortex ring, vortical structure, instability, turbulent state.

1 Introduction

Vortex rings widely exist in nature and engineering and can be considered as one typical vortex motion [1]. The interaction of vortex ring with a solid wall has also received

*Corresponding author. *Email address:* xlu@ustc.edu.cn (X.-Y. Lu)

 ©2015 Global-Science Press

https://doi.org/10.4208/cicp.150115.210715s Published online by Cambridge University Press

considerable attention as discussed below for extensive work. When the Reynolds number (Re) based on the translational speed and initial diameter of the vortex ring is high enough, the interaction can lead to the breakdown of vortex rings and transition to turbulent state [2–4]. Thus, various fundamental mechanisms dictating the relevant flow behaviors are still completely unclear, in particular for the high-Reynolds-number vortical flow, and are of great interest for further detailed studies.

Vortex ring interacting with a flat wall has been studied numerically and experimentally [2, 5–12]. As the primary vortex ring evolves toward the wall, its approach rate slows and its radius increases gradually in accompany with the generation of secondary vorticity on the wall. When the Reynolds number is larger than about 500 [9,11], the secondary vortex separates from the surface and interacts with the primary vortex ring resulting in the ring rebounding from the wall. Actually, these studies described above are mainly limited to relatively low-Reynolds-number flow regime and the highest Reynolds number in these studies is about 2840 [2]. The experimental study has revealed that the primary vortex ring no longer remains stable as it approaches the wall at high Reynolds number [2]. Thus, the instability of vortex rings and transition to turbulence need to be investigated for a vortex ring impinging on a wall in the high-Reynolds-number regime.

The evolution of a free vortex ring is a prototypical vortical flow relevant to some fundamental behaviors, such as growth, instability, breakdown and transition of vortex ring. Extensive investigations have been carried out theoretically [13–16], experimentally [17–23], and numerically [24–27]. Krutzsch [13] first studied the instability of vortex ring and found that the vortex ring becomes unstable with some stationary waves distributed around its azimuthal direction. Crow [14] investigated the aircraft trailing vortices and presented the development process of the vortex instability. Then Maxworthy [17–19] and Widnall [20] verified experimentally that the stationary azimuthal waves grow in the surface at 45° relative to the propagation direction of vortex ring, and the wave number depends on the slenderness ratio of core radius to ring radius. Widnall and Tsai [16] gave the theoretical explanation of the instability and indicated that a straining field in the neighbourhood of the vortex core leads to the amplification of small perturbation. Shariff et al. [25] established a viscous correction to the growth rate in terms of their direct numerical simulation (DNS) results. Dazin et al. [21,22] experimentally investigated the linear and nonlinear stages of vortex ring decay and found that the straining field causes the instability. Bergdorf et al. [26] numerically studied the evolution of vortex rings at $Re_\Gamma = 7500$ based on the circulation of the vortex ring and demonstrated the formation of a series of hair-pin vortices during the early turbulent stage. Archer et al. [27] further investigated the effects of Reynolds number and core thicknesses on the vortex ring evolution from laminar to the early turbulent regime and indicated that the onset of the turbulent state is associated with the formation of a series of hairpin vortices.

Compared with the studies of the instability of free vortex rings, the investigation relevant to the instability of a vortex ring impinging on a wall is still scarce. Walker et al. [2] experimentally investigated the trajectories of vortical structures for $564 \leq Re \leq 2840$. At

https://doi.org/10.4208/cicp.150115.210715s Published online by Cambridge University Press

lower Reynolds number, rebounding of the primary vortex is observed. At intermediate Reynolds number, two occurrences of rebounding and reversal of the primary vortex are identified. At higher Reynolds number, the wave-like instability of vortical structures is generated and the ejection of secondary vortex ring is formed. Orlandi and Verzicco [3] numerically analyzed the azimuthal instabilities at $Re=1250$ by imposing an initial azimuthal perturbation on the primary vortex ring and identifying a response perturbation in the secondary ring. Swearingen et al. [28] investigated the evolution and instability of both perturbed and unperturbed secondary vortex rings at $Re=645$ using quasi-steady and long-wavelength approximations and found that the instability depends on the position of the secondary ring relative to the primary ring and the ratio of the primary and secondary ring circulations. Archer et al. [4] then studied a laminar vortex ring impacting a free surface using DNS and found that the instability transfers from short-wavelength instability to long-wavelength instability. The transfer happens through the rotation of wavy inner core structure and the shedding of outer core vorticity. Recently, Masuda et al. [29] and Yoshida et al. [30] experimentally studied the interaction of a vortex ring with a granular layer at $1500 \leq Re \leq 4100$ and revealed that the wavy secondary vortex ring develops into hair-pin vortices which then wrap around the primary vortex ring in the late stage of the interaction.

For the vortex evolution with its transition to turbulence at large Reynolds number, large eddy simulation (LES) has provided a useful tool for studying such the vortical flow behaviors from laminar to turbulent regime. Sreedhar and Ragab [31] used LES to investigate the response of longitudinal stationary vortices subject to random perturbations for the Reynolds number 10^5 based on the maximum initial tangential velocity and the core radius. Mansfield et al. [32] employed Lagrangian LES to simulate the collision of coaxial vortex rings and captured several distinctive phenomena, including the development of azimuthal perturbations, strong interaction between the vortex cores, and the generation of small-scale turbulent structures. Faddy and Pullin [33] studied the flow structures of a pair of counter-rotating vortices and performed the simulations using DNS at low Reynolds number 10^3 and LES at high Reynolds number 2×10^4, where the Reynolds number is based on the circulation of the Lamb-Oseen vortex.

In this paper, an LES technique is utilized to investigate the dynamics and instability of a vortex ring impinging on a wall for two typical vortex core thicknesses at a Reynolds number 4×10^4 based on the translational speed and initial diameter of the vortex ring. The purpose is to achieve an improved understanding of some fundamental phenomena involved in this vortical flow, including evolution of vortical structures, formation of vortices wrapping around vortex rings, instability and breakdown of vortex rings, and transition from laminar to turbulent state.

This paper is organized as follows. The mathematical formulation and numerical methods are briefly presented in Section 2. The computational overview and validation are described in Section 3. Detailed results are then given in Section 4 and the concluding remarks in Section 5.

https://doi.org/10.4208/cicp.150115.210715s Published online by Cambridge University Press

2 Mathematical formulation and numerical methods

To investigate a vortex ring impinging on a flat wall, the three-dimensional Favre-filtered compressible Navier-Stokes equations in generalized coordinates are used. The equation of state for an ideal gas is used and the molecular viscosity is assumed to obey the Sutherland law. To non-dimensionalize the equations, we use the far-field variables and the initial radius of vortex ring as characteristic scales. Following the previous approach, such as an LES on the evolution of longitudinal stationary vortices [31,34] and an LES of turbulent swirling flows injected into a dump chamber [35], it should be indicated that the present simulations are for a low-Mach-number flow based on the far-field speed of sound which is very near the incompressible limit. This approach has been verified to reliably predict the incompressible flow characteristics of the vortex evolution [31,34].

In the present LES for turbulence closure, some terms in the Favre-filtered equations arising from unresolved scales need to be modelled in terms of resolved scales. Then, dynamic subgrid-scale (SGS) models for turbulent flows are employed. A detailed description of the mathematical formulation of the equations and the SGS models can be found in our previous papers [35,36].

The governing equations are numerically solved by a finite-volume method. As employed in our previous work [36–38], the convective terms are discretized by a second-order centered scheme and the viscous terms by a fourth-order central scheme. The time advancement is performed using an implicit approximate-factorization method with subiterations to ensure the second-order accuracy.

3 Computational overview and validation

3.1 Computational overview

As shown in Fig. 1 for the sketch of a vortex ring impacting on a wall, the vortex ring with radius R_0 is initially placed at $\boldsymbol{x_c}=(0,0,H)$, where H is the distance between the vortex ring centre and the wall. The initial vorticity distribution of the vortex ring is assigned by a Gaussian function [25] and the initial translational speed of the ring can be estimated as [39]

$$u_s=\frac{\Gamma_0}{4\pi R_0}\left(\ln\frac{8R_0}{\sigma_0}-\frac{1}{4}\right), \tag{3.1}$$

where σ_0 is the initial core radius and Γ_0 is the initial circulation of vortex ring. To deal with the instability of the vortex ring, an azimuthal disturbance is introduced by imposing a radial displacement on the axis of the ring and the local radius $R(\theta)$ can be expressed as [27]

$$R(\theta)=R_0[1+\zeta g(\theta)],$$

https://doi.org/10.4208/cicp.150115.210715s Published online by Cambridge University Press

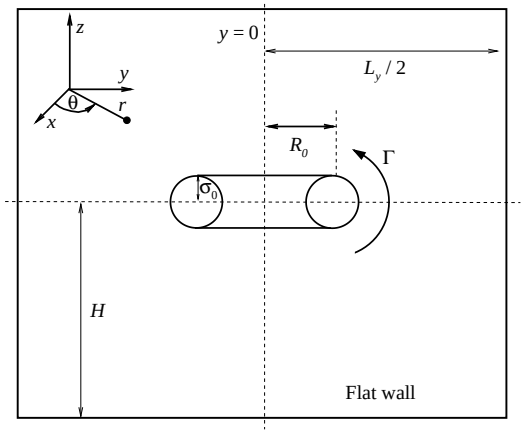


Figure 1: Schematic diagram of a vortex ring approaching a flat wall.

$$g(\theta)=\sum_{n=1}^{N} A_n \sin(n\theta)+B_n\cos(n\theta),$$

where ζ is a small parameter and is chosen as 2×10^{-4} by following the previous selection [26,27], and $g(\theta)$ represents the sum of a set of N Fourier modes with $N=32$ used here.

In the present study, we consider two typical cases for thin and thick vortex rings with the slenderness ratio $\sigma_0/R_0=0.2$ and 0.4, respectively. For both the cases, the Reynolds number based on the initial translational speed and diameter of the vortex ring is $Re=4\times10^4$. Correspondingly, the Reynolds number based on the initial circulation of the vortex ring is $Re_\Gamma=7.3\times10^4$ and 9.2×10^4 for the thin and thick rings.

According to our tests, the computational domain extends for $16R_0$ in the x- and y-directions and $12R_0$ in the vertical or z-direction, i.e. $L_x=L_y=16R_0$ and $L_z=12R_0$. The grid-spacing is uniform in the x- and y-directions, and grid stretching is employed in the z-direction to increase the grid resolutions near the wall surface. The minimum size of the grid is $\Delta z=10^{-5}R_0$. It is ensured that there are at least 40 nodes in the vorticity thickness on the wall in the attached boundary-layer region. The vortex ring is initially placed at $H=6R_0$. The time step is chosen as $\Delta t=0.0025$. Following the previous treatment [4,28], periodic boundary conditions are used in the x- and y-directions. The computational domain chosen in the present study, which is larger than ones used in the previous work [4,28], is sufficiently large to ensure that the effects of the periodicity are very small. No-slip boundary condition is employed on the wall and a far-field boundary condition is applied at $z=L_z$.

To clearly present the post-processing, the averaging operation and coordinate transformation are performed in terms of the time-dependent resolved density $\bar{\rho}$, pressure $\bar{p}$ and velocity $\bar{u}_i$ obtained in the simulation. The symbol $\langle\ \rangle$ represents the average in the azimuthal direction after transforming the data from the Cartesian coordinate system (x,y,z) into the cylindrical coordinate (r,θ,z) as shown in Fig. 1.

https://doi.org/10.4208/cicp.150115.210715s Published online by Cambridge University Press

3.2 Code validation

To assess the effect of grid resolution on the calculated results for the present problem, three test cases for the thin vortex ring have been examined. Fig. 2 shows the distributions of the azimuthally averaged pressure coefficient defined by $\langle C_p\rangle = R_0^2(\langle\bar{p}\rangle - p_\infty)/(\langle\bar{\rho}\rangle\Gamma_0^2)$ along the radial direction at $t=22.5$, where p_∞ represents the far-field pressure. Noted that the instant $t=22.5$ approximately corresponds to the formation of secondary ring after the primary ring collides with the wall, which is sensitive to the grid resolutions. As shown in Fig. 2, the results for cases 2 and 3 collapse together, indicating a reasonable convergence for the grid resolution. To make the prediction accurate, the finest gird $641\times 641\times 381$ as indicated in Fig. 2 is used in the present simulation.

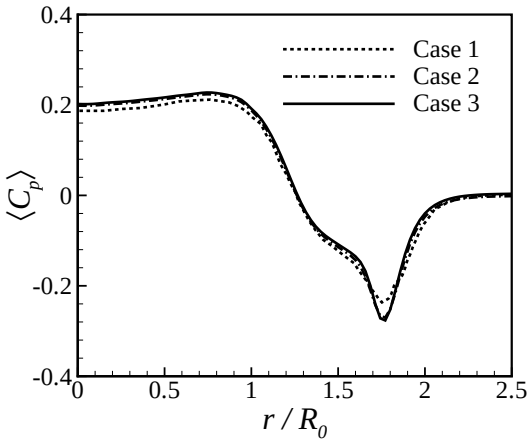


Figure 2: Comparison of the azimuthal mean pressure coefficient on the wall for three test cases with different grid resolutions for the thin vortex ring at $t=22.5$. The grid resolution is $N_x\times N_y\times N_z = 481\times 481\times 281$ for case 1, $561\times 561\times 321$ for case 2 and $641\times 641\times 381$ for case 3, where N_x, N_y and N_z represent the grid number in the x, y and z directions, respectively.

To validate the present simulation, we first consider a thin vortex ring ($\sigma_0/R_0=0.21$) impacting a wall at Re=830, which has been investigated experimentally and numerically [8, 11]. Fig. 3 typically shows the trajectory of the primary ring centre obtained in this study and the previous results for comparison. It is seen that our results agree well with the experimental data [8] and numerical results [11].

Then, we investigate the instability of free thin and thick vortex rings and compare with the numerical results of Shariff et al. [25] and Archer et al. [27]. As listed in Table 1 for the two vortex rings, we have obtained the wave number of most amplified mode k=9 for the thin ring and $k=6$ for the thick ring, which are the same as the previous results [25,27]. Moreover, the agreement is also established in Table 1 by comparison the present most growth rate with the previous results obtained by Shariff et al. [25] and Archer et al. [27], respectively, where the growth rate for mode k is defined as $\alpha_k=(dE_k/dt)/(2E_k)$ with E_k the perturbation energy of the mode.

https://doi.org/10.4208/cicp.150115.210715s Published online by Cambridge University Press

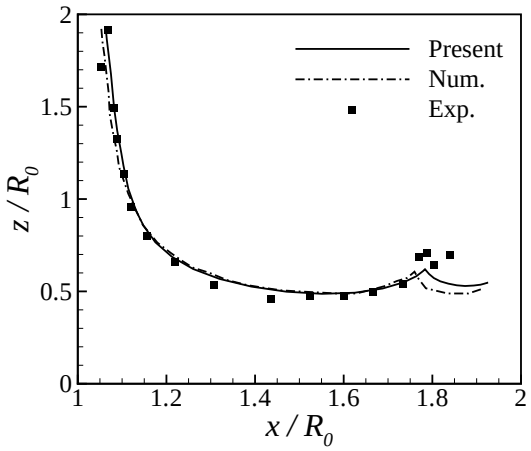


Figure 3: Trajectory of the primary ring centre at $Re=830$. The solid and dashdot lines denote the numerical results by the present simulation and by Cheng et al. [11], respectively. The symbols represent the experimental data of Chu et al. [8].

Table 1: Comparison of the present most growth rate α with the previous results denoted by α_S for Shariff et al. [25] and by α_A for Archer et al. [27].

Case	σ_0/R_0	Re_Γ	t	$k(t)$	α	α_S	α_A
A	0.200	7500	52.5	9	0.114	0.119	0.112
B	0.413	5500	52.5	6	0.077	0.090	0.072

Moreover, the present numerical strategy has already been applied with success to a wide range of turbulent flows [35–38]. We have carefully examined the physical model and numerical approach used in this study and verified that the calculated results at high Reynolds number are reliable.

4 Results and discussion

4.1 Vortical structures for thin and thick vortex rings

The flow field involves an array of complicated flow phenomena, such as the generation of secondary and tertiary vortex rings, the interaction and deformation of vortex rings, the instability and breakdown of vortex rings, and the transition to turbulent state. To assess the existence of vortical structures in the flow field, these phenomena are elucidated for thin and thick vortex rings. Moreover, in order to neatly demonstrate the evolution of vortical flow, we may divide the evolution into three typical stages based on the calculated results, i.e. approach and slowing, collision and breakdown, and turbulent state, which will be described below.

https://doi.org/10.4208/cicp.150115.210715s Published online by Cambridge University Press

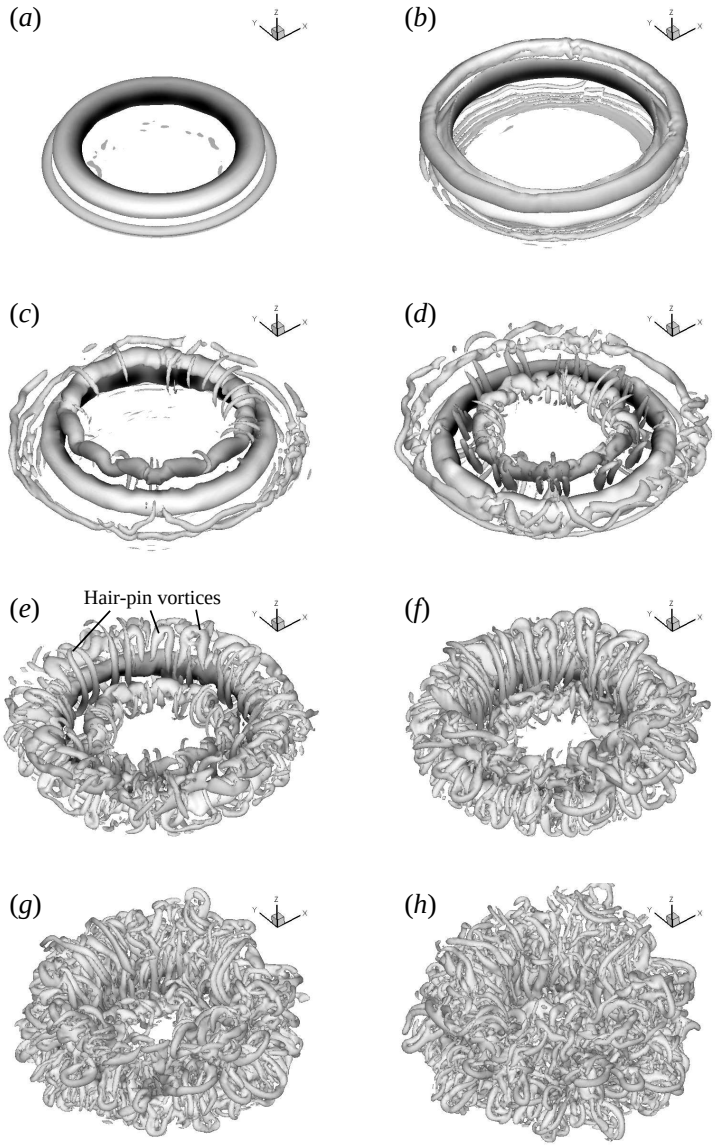


Figure 4: Evolution of vortical structures visualized by an isosurface of the Q criterion with $Q=1$ for thin vortex ring: (*a*) $t=22.5$, (*b*) 25.0, (*c*) 27.5, (*d*) 30.0, (*e*) 32.5, (*f*) 35.0, (*g*) 37.5, (*h*) 40.0.

The evolutions of vortical structures for the thin vortex ring are shown in Fig. 4. Here, the vortical structures are depicted by isosurface of the Q criterion described as $Q=-\frac{1}{2}(||\boldsymbol{S}||^2-||\boldsymbol{\Omega}||^2)$, where $\boldsymbol{S}$ and $\boldsymbol{\Omega}$ denote the strain and the rotation tensor, respectively. A positive value of Q presents the regions in which the rotation exceeds the strain. Thus, the instantaneous vortical structures depicted by $Q=1$ are illustrated in Fig. 4. Correspondingly, to clearly demonstrate the evolution of the primary and its induced

https://doi.org/10.4208/cicp.150115.210715s Published online by Cambridge University Press

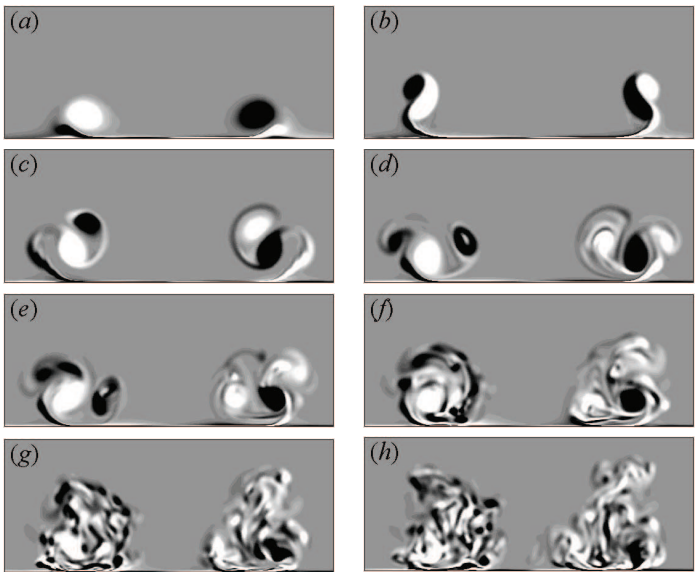


Figure 5: The azimuthal vorticity component ω_θ in the $y=0$ meridian plane for the thin vortex ring: (*a*) $t=22.5$, (*b*) 25, (*c*) 27.5, (*d*) 30, (*e*) 32.5, (*f*) 35, (*g*) 37.5, (*h*) 40.

secondary and tertiary vortex rings, Fig. 5 shows the azimuthal vorticity component ω_θ in the $y=0$ meridian plane.

From Figs. 4 and 5, when the vortex ring moves close to the wall, a thin vorticity layer is generated on the wall. The stretching and deformation of the primary ring occur. Then, the formed vorticity layer on the wall grows rapidly due to the radially adverse pressure gradient induced by the primary ring and results in the generation of secondary vortex ring and lifting up from the wall as shown in Figs. 4(*a*) and 5(*a*). The interaction of the secondary and primary rings decelerates the expansion of the primary ring and induces the primary ring to rebound from the wall in Figs. 4(*b*) and 5(*b*). Then, the secondary ring penetrates into the interior of the primary ring as shown in Figs. 4(*c*,*d*) and 5(*c*,*d*). Moreover, due to the growth of the azimuthal perturbation, the primary and secondary rings evolve into wavy-like structures in Fig. 4(*c*,*d*). A tertiary vortex ring and the induced vorticity layer separated from the wall are also formed. As shown in Figs. 4(*e*) and 5(*e*), the secondary ring begins to interact with the wall. In the above process, the strong azimuthal instability leads to the large deformation of the secondary ring. The strength and wave number of the azimuthal instability of primary and secondary rings will be analyzed in detail in Section 4.3. Moreover, it is observed from Figs. 4(*d*) and 4(*e*) that a series of loop-like vortices [40–42] and hair-pin vortices [43–45] wrapping around the vortex rings are formed, which are briefly called wrapping vortices in the following discussion. With the evolution of vortical structures, it is seen that the strength and number of the wrapping vortices are increased considerably as shown in Figs. 4(*e*-*g*). Finally, the complicated interactions of the vortex rings, the wrapping vortices and the wall lead

https://doi.org/10.4208/cicp.150115.210715s Published online by Cambridge University Press

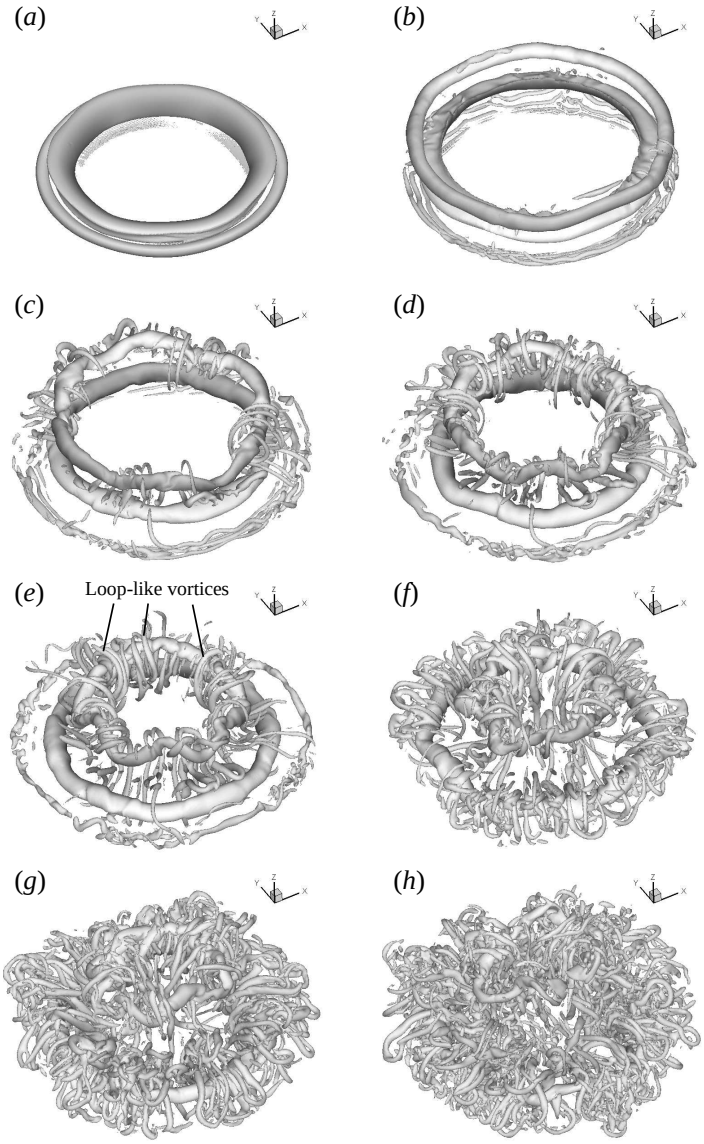


Figure 6: Evolution of vortical structures visualized by an isosurface of the Q criterion with $Q=1$ for the thick vortex ring: (*a*) $t=27.5$, (*b*) 32.5, (*c*) 35, (*d*) 37.5, (*e*) 40, (*f*) 45, (*g*) 50, (*h*) 55.

to the vortical structures breakdown into the small-scale vortices as shown in Figs. 4(*h*) and 5(*h*) and further result in the vortical flow transition to turbulent state which will be analyzed in Sections 4.3 and 4.4.

To elucidate the effect of the core thicknesses on the evolution of flow structures, Figs. 6 and 7 show the vortical structures in terms of the Q criterion and the azimuthal vorticity component ω_θ in the y=0 meridian plane for the thick vortex ring. It is seen from

https://doi.org/10.4208/cicp.150115.210715s Published online by Cambridge University Press

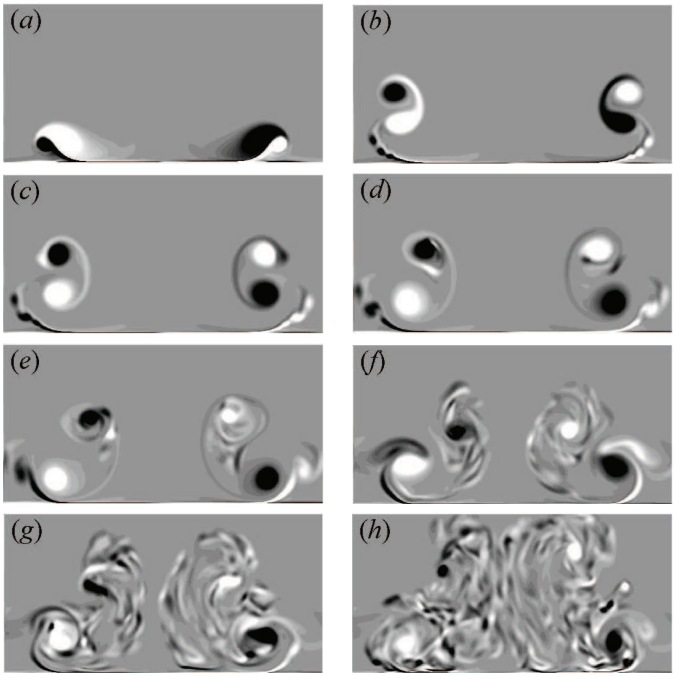


Figure 7: The azimuthal vorticity component ω_θ in the $y=0$ meridian plane for the thick vortex ring: (*a*) $t=27.5$, (*b*) 32.5, (*c*) 35, (*d*) 37.5, (*e*) 40, (*f*) 45, (*g*) 50, (*h*) 55.

Figs. 6(*a*) and 7(*a*) that the secondary ring is formed on the wall, which is qualitatively similar to the generation of the thin ring case described above. Then, from Figs. 6(*b*-*e*) and 7(*b*-*e*), the secondary ring evolves away from the wall and gradually shrinks over the primary ring. Correspondingly, the azimuthal instabilities of the primary and secondary rings are strengthened and the wrapping vortices are enhanced during the evolution in Figs. 6(*c*-*g*). Furthermore, the complicated interactions of these vortices induce the breakdown of vortices, such as in Figs. 6(*h*) and 7(*h*), and result in the flow transition to turbulent state.

Compared with the evolution of vortical structures for the thin and thick vortex rings, it is noticed that the secondary ring moves toward the wall for the thin ring and away from the wall for the thick ring, consistent with the experimental finding [2]. The different properties are associated with the circulation strengthes of the secondary ring which will be analyzed below. Moreover, the temporal development of a series of wrapping vortices for the thin vortex ring is faster than that for the thick vortex ring. This behavior indicates that the instability for the thin ring evolves faster than one for the thick ring, consistent with the prediction of free vortex rings [27].

Further, the formation process of the wrapping vortices and the relevant mechanism are analyzed. It is observed from Figs. 4 and 6 that the loop-like and hair-pin vortices wrapping around the vortex rings are formed, which play an important role in the flow evolution from laminar to turbulent state [27, 34]. We can identify that the hair-pin vor-

https://doi.org/10.4208/cicp.150115.210715s Published online by Cambridge University Press

tices mostly occur for the thin ring case as typically shown in Fig. 4(*e*,*f*), and the loop-like vortices mostly appear for the thick ring case as shown in Fig. 6(*e*,*f*). The relevant physical mechanism is related to the secondary ring movement, i.e. moving toward the wall for the thin ring and moving away from the wall for the thick ring as described above. The formation of the wrapping vortices is essentially associated with the deformation of vortex rings induced by the strong azimuthal instability. Moreover, the hair-pin vortices are evolved by the reconnection of loop-like vortices and by the stretching and deformation of the tertiary vortex ring when the secondary ring moves towards the wall for the thin ring case. The instability causes displacement of the inner core into a wave-like pattern. Then the wrapping vortices are gradually formed in the wave-like location. Thus the thin vortex ring generates more loop-like vortices than the thick ring. As discussed above, the generation of hair-pin vortices is associated with the loop-like vortices and the azimuthal instability of the tertiary vortex ring, and more loop-like vortices and more wave number of the vortex ring for the thin case must lead to more hair-pin vortices than the thick case.

4.2 Trajectory and circulation of vortex ring and axial flow of vortex core

To investigate the global behavior of flow evolution, we further investigate the trajectories and circulations of the primary and secondary vortex rings. The location of vortex ring is determined by its centre in the mean azimuthal (r,z) plane which is expressed as [27,39]

$$r=\frac{1}{\Gamma}\int r\langle\omega_\theta\rangle drdz,\quad z=\frac{1}{\Gamma}\int z\langle\omega_\theta\rangle drdz, \tag{4.1}$$

where $\langle\omega_\theta\rangle$ represents the mean azimuthal vorticity and Γ is the circulation which can be obtained by [46]

$$\Gamma=\int\langle\omega_\theta\rangle drdz. \tag{4.2}$$

The trajectories of the primary and secondary rings are shown in Fig. 8(*a*). When the vortex ring is far from the wall, the motion of the primary ring is little affected by the wall and the radius of the vortex ring remains nearly constant. As the primary ring moves near the wall, the influence of the wall becomes significant, which reduces the translational velocity of the ring and causes the radius to expand quickly. Then, when the collision between the vortex ring and wall happens, the primary ring is subject to two reversal rotations induced by the secondary ring for both the thin and thick ring cases, consistent with experimental findings [2]. Moreover, Fig. 8(*a*) also shows the trajectories of the secondary rings. The secondary ring evolves around the primary ring for the thin ring case and moves away from the wall for the thick ring case, as demonstrated by the evolution of vortical structures in Figs. 4 and 6.

Fig. 8(*b*) shows the circulations of the vortex rings. Based on the profiles of the primary rings and the evolution of vortical structures in Figs. 4 and 6, the process of the

https://doi.org/10.4208/cicp.150115.210715s Published online by Cambridge University Press

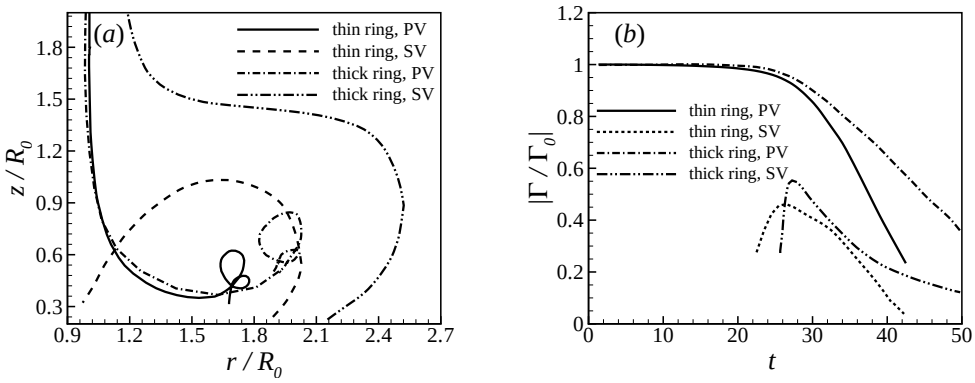


Figure 8: Trajectories and circulations of vortex rings: (*a*) trajectories of primary and secondary rings; (*b*) evolution of the circulations of vortex rings. Here, PV and SV represent the primary and secondary vortex rings, respectively.

interaction of the vortex ring and wall can be divided into three distinct stages as indicated above, i.e. approach and slowing, collision and breakdown, and turbulent state. Here we mainly discuss the thin ring case. In the approach and slowing stage, the circulation is almost constant for $t<20$ as the primary ring is far from the wall and begins to decay slowly for approximately $20<t<24$. Then, in the collision and breakdown stage, a rapid decay of the circulation occurs due to the breakdown of vortex rings. Furthermore, when the flow evolves as turbulent state around $t>40$ which will be discussed in Section 4.4, an approximately linear decay of the circulation is exhibited. On the other hand, it is also obtained from Fig. 8(*b*) that the circulation for the thick ring decays slowly with respect to the thin ring case and the three typical stages are similar to the thin ring case.

As shown in Fig. 8(*b*) for the circulations of the secondary rings, the circulation increases rapidly after the secondary ring is generated on the wall. It is seen that the peak value of circulation for the thick secondary ring at approximately $t=27.5$ is stronger than that for the thin secondary ring at $t=26$. This implies that the self-induced velocity of the secondary ring which causes its moving upward is larger than the induced velocity by the primary ring, resulting in the secondary ring moving away from the wall for the thick ring case as shown in Fig. 8(*a*). Moreover, the circulation of the secondary ring for the thick ring case decays more slowly than that for the thin ring case, which is similar to the behavior of the primary ring.

Further, the axial flow which represents the circumferential flow along the axis of the vortex core [19] is investigated because it is related to the vortex ring evolution to turbulent state [27]. As the axial flow reaches maximum at the centre of vortex core, the axial flow $u_{\theta m}$ and the core centre can be determined by the interpolation from the local azimuthal velocity u_θ. Fig. 9 shows the azimuthal distributions of axial flow of the primary ring for the thin and thick rings. As shown in Fig. 9(*a*) for the thin ring, the amplitude of $u_{\theta m}$ is relatively small at $t=10$ and grows quickly to generate a pronounced axial flow, such as at $t=30$ and 35. It is also seen that the number of wave-like curve

https://doi.org/10.4208/cicp.150115.210715s Published online by Cambridge University Press

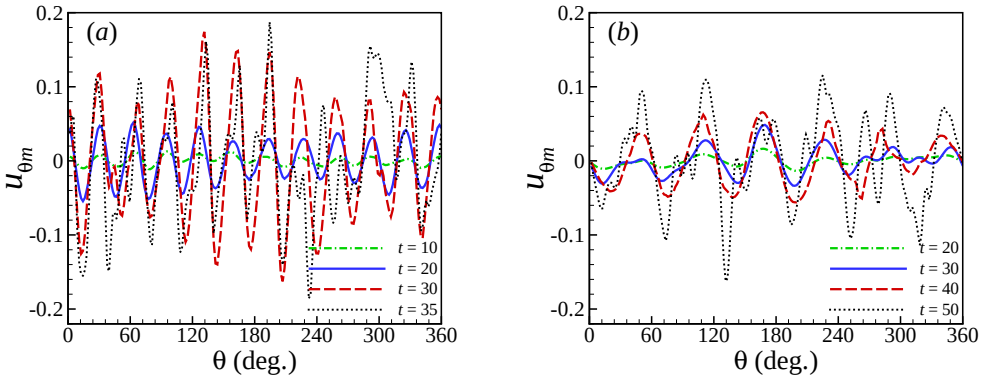


Figure 9: Axial flow of primary vortex rings: (*a*) thin vortex ring, (*b*) thick vortex ring.

is 11, consistent with the wave number of dominant azimuthal mode $k=11$ which will be analyzed in the following subsection. Thus the generation of the axial flow is related to the azimuthal instability. Further, as shown in Fig. 9(*b*) for the thick ring, the axial flow grows quickly and the number of wave-like curve is also consistent with the wave number of dominant azimuthal mode $k=6$. Compared to the temporal evolution of the axial flow for the thin and thick rings, it is reasonably identified that the growth rate of axial flow for the thin ring is faster than that for the thick ring. Furthermore, the axial flow should be due to an azimuthal pressure gradient [47], which is associated with the growth of azimuthal instability and the core stretching of vortex ring.

4.3 Instability of vortex ring and modal energies

The evolution of vortex ring and the formation of axial flow are related to the azimuthal instability based on the instability analysis of a free vortex ring [25] and of a vortex ring impinging on a free surface [4]. For the present problem, we further investigate the instability of primary and secondary vortex rings and the transition to turbulence of the vortical flow evolution.

The perturbation growth relevant to the azimuthal instability is first investigated in the early stage of a vortex ring impinging on a wall. Based on the previous analysis [4, 25], we use the root mean square value of the azimuthal velocity of vortex ring (i.e. $u_{\theta rms}$) to indicate the alignment of the wavy perturbation. Fig. 10 shows the contours of $u_{\theta rms}$ for the thin ring. At $t=15$ in Fig. 10(*a*), the ring is somewhat far away from the wall. It is reasonably obtained that the plane in which the structure aligns is inclined at approximately 45° to the direction of ring propagation, which is consistent with the experimental and numerical findings for a free vortex ring [17, 25]. Then, as the vortex ring evolves to the wall, the plane gradually rotates with an inclined angle from 55° at $t=20$ to 68° at $t=25$ in Fig. 10(*b*,*c*) due to the wall effect. From the contour values, the magnitude of $u_{\theta rms}$ increases, indicating the perturbation growth during the vortex

https://doi.org/10.4208/cicp.150115.210715s Published online by Cambridge University Press

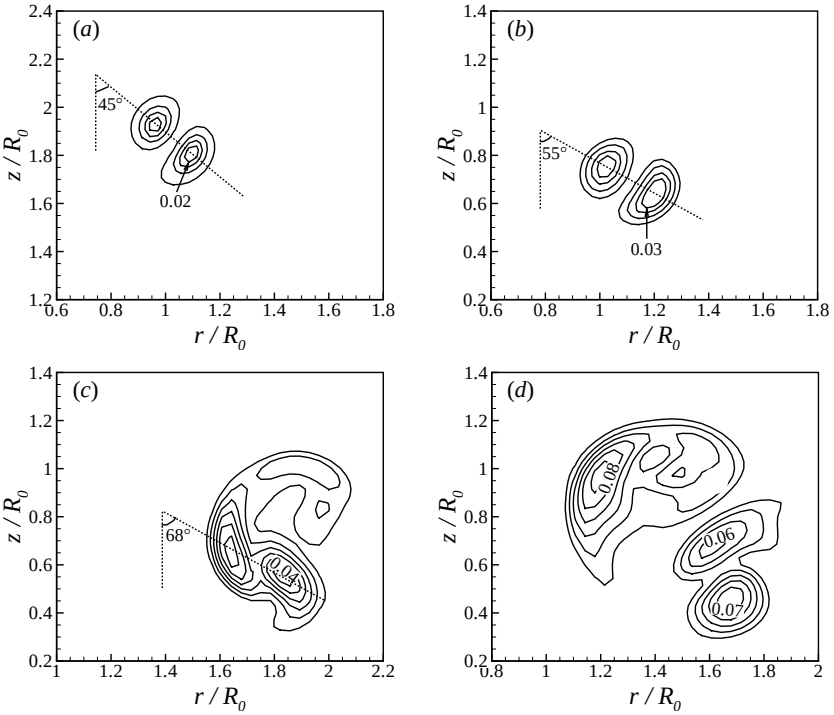


Figure 10: Evolution of $u_{\theta rms}$ for the thin vortex ring: (a) $t=15$, (b) 20, (c) 25, (d) 27.5.

ring evolution. Furthermore, the perturbation of $u_{\theta rms}$ for the secondary vortex ring is apparent in Fig. 10(c,d) at $t=25$ and 27.5, corresponding to the vortical structures in Fig. 4(b,c). The amplitude of $u_{\theta rms}$ for the secondary ring is larger than one for the primary ring in Fig. 10(d), indicating that the perturbation growth is faster for the secondary ring.

To quantitatively study the characteristics of azimuthal instabilities, we further perform the Fourier analysis of the vertical vorticity $\omega_z(r,\theta,z)$ [48]. For each r–θ plane, the azimuthal component decomposition of ω_z is expressed as

$$\omega_k(r,\theta,z,t)=C_k(r,z,t)\cos(k\theta)+S_k(r,z,t)\sin(k\theta), \tag{4.3}$$

where $C_k(r,z,t)$ and $S_k(r,z,t)$ represent the Fourier coefficients defined by

$$\{C_k(r,z,t),S_k(r,z,t)\}=\frac{1}{\pi}\int_0^{2\pi}\omega_z(r,\theta,z,t)\{\cos(k\theta),\sin(k\theta)\}d\theta. \tag{4.4}$$

Based on the decomposition, a measure of the amplitude of the azimuthal component of ω_z for each wave number on a vertical plane is given as [49]

$$A_k(z,t)=\left(\int_0^{2\pi}\int_0^{\infty}\omega_k^2(r,\theta,z,t)rdrd\theta\right)^{\frac{1}{2}}. \tag{4.5}$$

https://doi.org/10.4208/cicp.150115.210715s Published online by Cambridge University Press

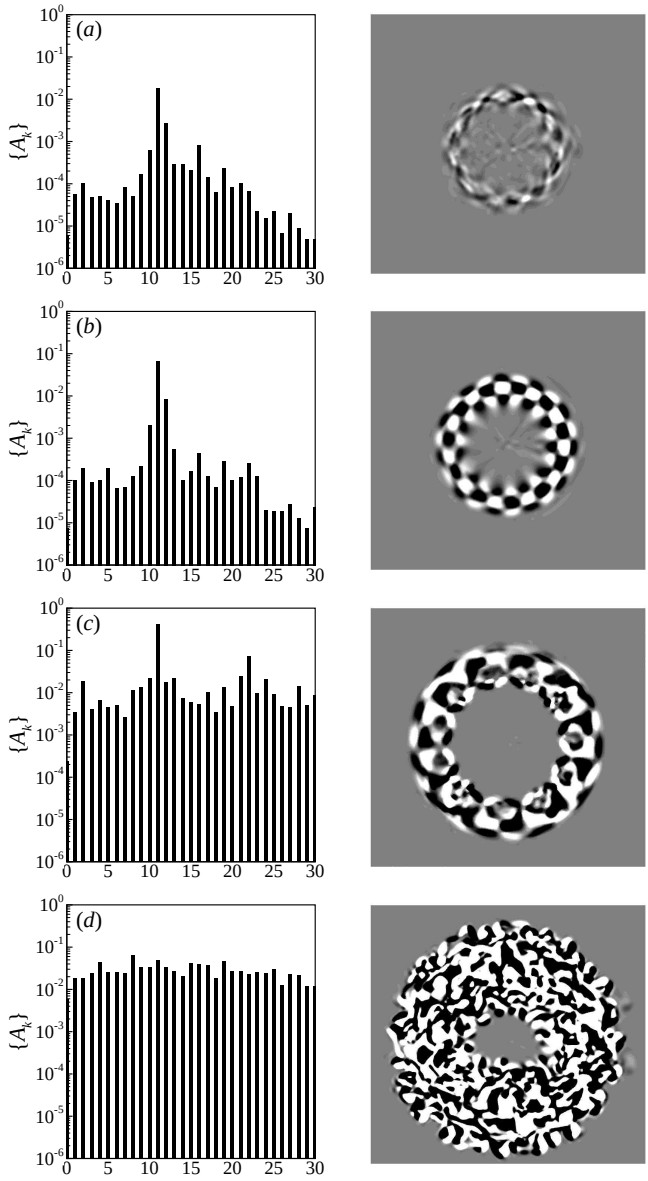


Figure 11: Development of the first 30 modes of primary vortex ring (left panel) and the patterns of wall-normal vorticity component (right panel) for the thin ring case: (*a*) $t=10$, (*b*) 20, (*c*) 27.5, (*d*) 35.

Then $\{A_k\}$ is calculated by local average in the vertical region of vortex ring, which denotes the azimuthal perturbation modes in the vortex ring.

To deal with the development of the azimuthal instabilities, Fig. 11 typically shows the distribution of $\{A_k\}$ and the pattern of ω_z in the (r,θ) plane of maximum magnitude of vorticity for the thin primary vortex ring. It is seen from Fig. 11(*a*) that the dominant

https://doi.org/10.4208/cicp.150115.210715s Published online by Cambridge University Press

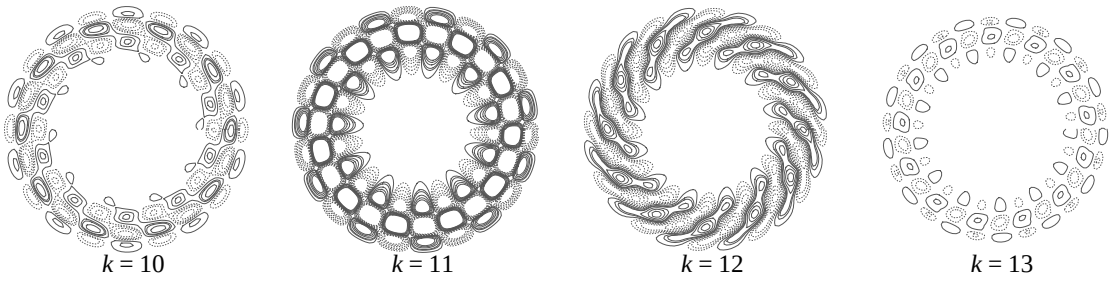


Figure 12: Several mode shapes of primary vortex ring for the thin ring case at $t=20$. The contours are plotted in the range of $|\omega_z|\leq 0.5$ with an increment 0.05.

mode is $k=11$, consistent with the theoretical estimate of the dominant mode approximately $k=2.26/\sigma_0$ [25]. The ω_z is relatively weak from the pattern of ω_z. With the evolution of the vortex ring, the ω_z increases rapidly as shown in Fig. 11(b), implying the rapid growth of the instability. Then, the superharmonic mode $k=22$ is apparent in the excitation of the unstable mode $k=11$ and the magnitudes of $\{A_k\}$ are amplified considerably for all the modes in Fig. 11(c). With the vortices breaking into small-scale ones as described above, the dominant and superharmonic modes decay rapidly and all the modes exhibit the same order of magnitude in Fig. 11(d), indicating the flow transition to turbulent state [26].

To ascertain the characters of unstable modes, Fig. 12 also shows several mode shapes of ω_z in the (r,θ) plane for the thin ring at $t=20$, corresponding to Fig. 11(b). The pattern at $k=11$ with the maximum magnitude corresponds to the dominant mode. It is also identified that all the modes in Fig. 12 exhibit the structure of the second radial mode marked by the two nodal lines in the radial direction, consistent with the numerical results [25, 27].

Furthermore, Fig. 13 shows the distribution of $\{A_k\}$ for the secondary vortex ring. The dominant mode of the azimuthal instability is identified as $k=11$ in Fig. 13(a), which is reasonably consistent with the primary ring. The superharmonic mode $k=22$ is excited in Fig. 13(b,c). Subsequently, all the modes nearly reach the same order of magnitude of $\{A_k\}$ in Fig. 13(d). Moreover, compared with Figs. 11(d) and 13(d), it is interesting to notice that the magnitudes of $\{A_k\}$ for the secondary ring are larger than those for the primary ring.

Figs. 14 and 15 show the distribution of $\{A_k\}$ of the thick primary and secondary vortex rings, respectively. As shown in Figs. 14(a) and 15(a), the dominant mode for both the rings is $k=6$, which is consistent with the theoretical estimate of the dominant mode $k=2.26/\sigma_0$ [25]. With the evolution of the vortex rings, the superharmonic mode $k=12$ is excited for both the rings and all the modes nearly reach the same order of magnitude of $\{A_k\}$ in Figs. 14(b) and 15(b), indicating the flow transition to turbulent state [26]. According to the temporal evolution, the development of the azimuthal instabilities is similar for both the thin and thick ring cases.

https://doi.org/10.4208/cicp.150115.210715s Published online by Cambridge University Press

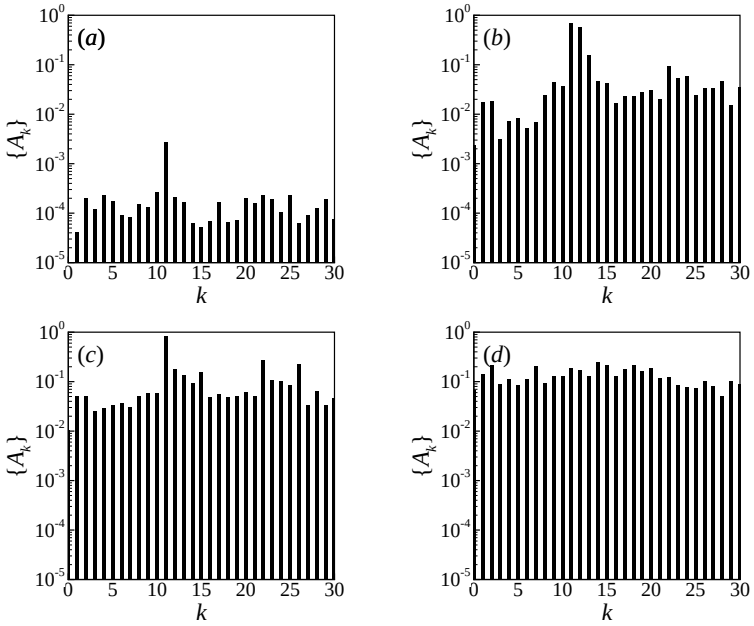


Figure 13: Development of the first 30 modes of secondary vortex ring for the thin ring case: (*a*) $t=25$, (*b*) 27.5, (*c*) 30, (*d*) 35.

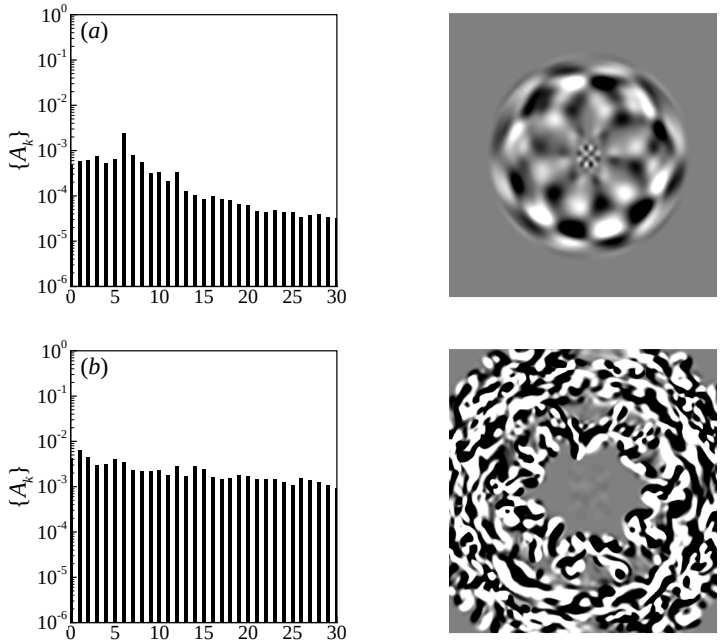


Figure 14: Development of the first 30 modes of primary vortex ring (left panel) and the patterns of wall-normal vorticity component (right panel) for the thick ring case: (*a*) $t=25$, (*b*) 45.

https://doi.org/10.4208/cicp.150115.210715s Published online by Cambridge University Press

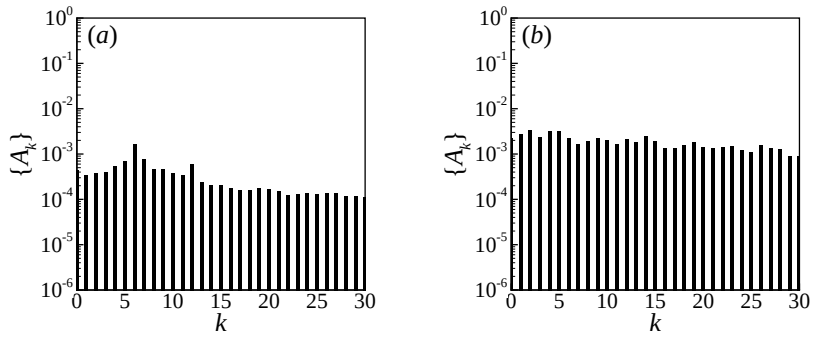


Figure 15: Development of the first 30 modes of secondary vortex ring for the thick vortex ring case: (*a*) $t=25$, (*b*) 45.

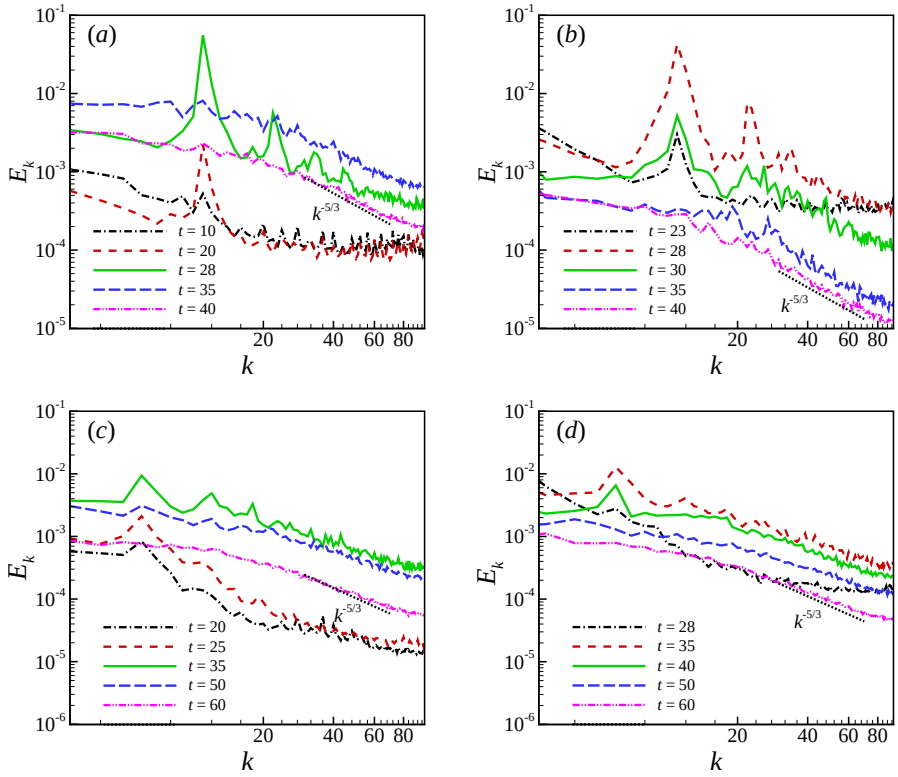


Figure 16: Development of modal energies at several typical times: (*a*,*c*) primary vortex ring, (*b*,*d*) secondary vortex ring; (*a*,*b*) thin vortex ring case, (*c*,*d*) thick vortex ring case.

To further investigate the behaviors relevant to the instability and breakdown of vortex rings, Fig. 16 shows the energy E_k in different azimuthal modes. As shown in Fig. 16(*a*) for the thin primary vortex ring, the modal energies are relatively weak at $t=10$ and a peak occurs for $k=11$ (i.e. dominant mode) at $t=20$. Then, the E_k is amplified

https://doi.org/10.4208/cicp.150115.210715s Published online by Cambridge University Press

considerably for all the modes and the peaks of superharmonic modes $k=22$, 33 and 44 are apparent at $t=28$. With the evolution of the vortex ring, the energies at the dominant mode and its superharmonic modes are transferred to other modes. The modal energies are amplified at $t=35$. As the vortices breaking into small-scale ones, the modal energies are gradually reduced at $t=40$. It is reasonably identified that the law of energy decay follows a characteristic $k^{-5/3}$ law, indicating that the vortical flow has become turbulent state [48,50]. Further, Fig. 16(*b*) shows the modal energies of secondary ring for the thin ring case. Similar to the development of modal energies of the primary ring, the dominant mode $k=11$ exhibits a peak at $t=23$ and its superharmonic modes are apparent at $t=28$. Then, the energy transfers among the modes with the vortical flow evolution and finally decays following the $-5/3$ power law at $t=40$.

The development of modal energies of the primary and secondary rings for the thick ring case is shown in Fig. 16(*c*,*d*). Similar to the thin ring case, the peaks of E_k reasonably correspond to the dominant mode $k=6$ and its superharmonic modes $k=12$ and 18. With the evolution of vortical flow, the energy decay follows the $-5/3$ power law, such as the profile at $t=60$. Moreover, it is seen that the peak values of dominant mode and its superharmonic modes for the thick ring are smaller than those for the thin ring, which is related to the fact that the instability growth for the thick ring is slower than that for the thin ring.

4.4 Flow behaviors in turbulent state

According to the preceding discussion, after the vortex rings breaking into small-scale vortices, the transition from laminar to turbulent state occurs. To investigate the flow evolution and the relevant turbulent behavior, we first analyze the total turbulent kinetic energy (TKE), which is defined as

$$\text{TKE}=\frac{1}{2}\int(\boldsymbol{u}'.\boldsymbol{u}')dV, \tag{4.6}$$

where $\boldsymbol{u}'$ represents the velocity fluctuations and is defined as $\boldsymbol{u}'=\bar{\boldsymbol{u}}-\langle\bar{\boldsymbol{u}}\rangle$, and the integral domain is the whole flow field.

Fig. 17(*a*) shows the evolution of TKE. For the thin ring, the TKE remains nearly zero and the flow is laminar state in the approach and slowing stage as discussed for the ring circulation in Fig. 8(*b*). Then, in the collision and breakdown stage, the TKE gradually grows at approximately $t=24$ and rapidly reaches its maximum at $t=40$, representing the flow transition to turbulence [31,34]. Subsequently, the TKE continuously decays due to viscous effect in the turbulent state. For the thick ring, the TKE evolves slowly with respect to the thin ring case and reaches its maximum at approximately $t=54$. Moreover, the strength of TKE for the thick ring is smaller than that for the thin ring, consistent with the behavior relevant to the modal energies in Fig. 16.

The formation and evolution of the vortices wrapping around the vortex rings, i.e. the loop-like and hair-pin vortices discussed above, play an important role in flow transition

https://doi.org/10.4208/cicp.150115.210715s Published online by Cambridge University Press

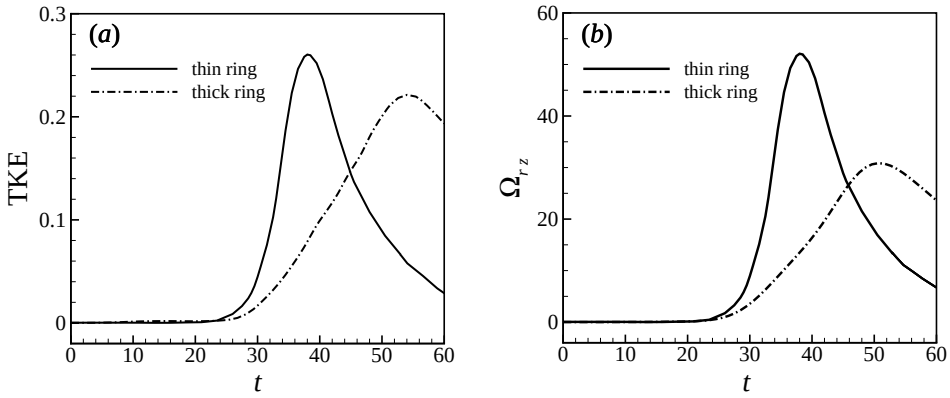


Figure 17: Evolution of (*a*) total turbulent kinetic energy and (*b*) enstrophy for the vortices wrapping around the vortex rings in the flow field.

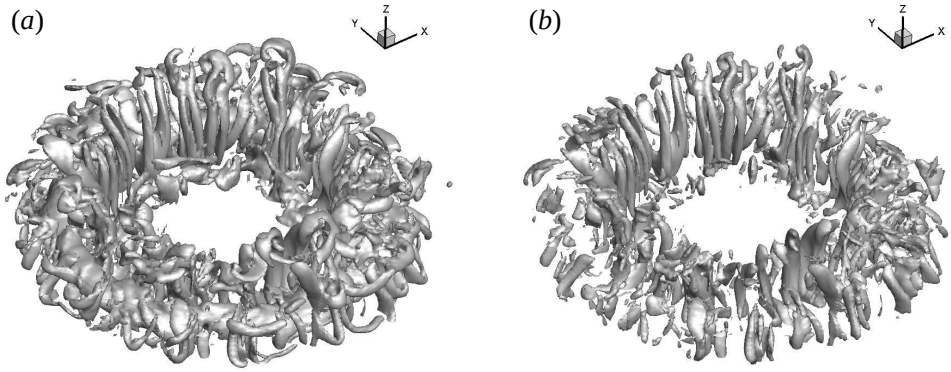


Figure 18: Vortical structures for the thin vortex ring at $t=35$ visualized by the vorticity magnitude (*a*) $|\omega|$ and (*b*) $(\omega_r^2+\omega_z^2)^{1/2}$.

from laminar to turbulent state. Here, we quantitatively examine the intrinsic connection of the wrapping vortices with the vortical flow evolution and transition to turbulence. Based on our careful analysis of the vortical structures, the wrapping vortices are mainly contributed by the vorticity components in the radial and vertical directions, i.e. ω_r and ω_z. As a typical case, Fig. 18 shows the vortical structures visualized by the vorticity magnitude $|\boldsymbol{\omega}|$ and $(\omega_r^2+\omega_z^2)^{1/2}$. It is seen that the vortical structure in Fig. 18(*b*) can reasonably represent the wrapping vortices exhibited in Fig. 18(*a*). We thus use the vorticity components ω_r and ω_z to essentially distinguish the wrapping vortices in this complicated vortical flow. Consequently, the strength of the wrapping vortices can be measured by the total enstrophy which is expressed as

$$\Omega_{rz}=\frac{1}{2}\int(\omega_r^2+\omega_z^2)dV. \tag{4.7}$$

https://doi.org/10.4208/cicp.150115.210715s Published online by Cambridge University Press

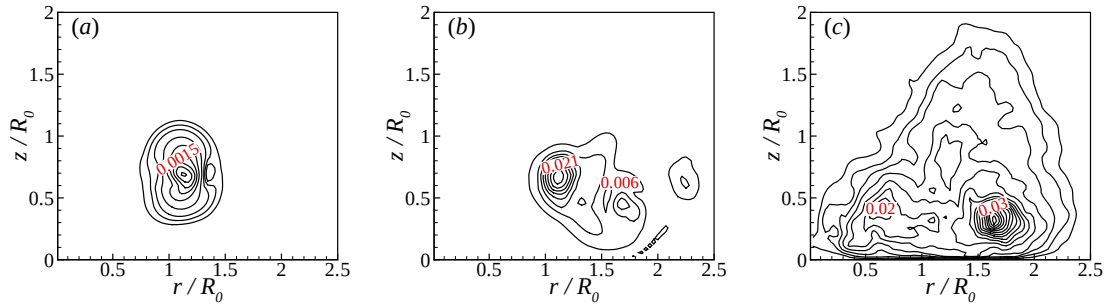


Figure 19: Contours of the azimuthal mean TKE for the thin vortex ring at several instants: (*a*) $t=20$, (*b*) 30, (*c*) 40.

Fig. 17(*b*) shows the evolution of Ω_{rz}. It is interesting to notice that the profiles of Ω_{rz} and TKE in Fig. 17(*a*) demonstrate the similar manner. The evolution of Ω_{rz} due to the loop-like and hair-pin vortices is accompanied with the variation of the TKE. This behavior confirms that there exists an intrinsic connection of the wrapping vortices with the vortical flow transition to turbulence.

To deal with the distribution of the TKE, Fig. 19 shows the contours of the azimuthal mean TKE for the thin ring case. It is seen that the TKE is mainly distributed in the core region of vortex rings. With the evolution of vortical flow, the TKE increases quickly and the distributed region expands gradually. Further, the azimuthal mean turbulent stresses are also calculated. It is reasonably identified that the normal stresses are obviously larger than the shear stresses and the azimuthal stress is the dominant component of the normal stresses.

5 Concluding remarks

Dynamics and instability of a vortex ring impinging on a wall were studied by means of large eddy simulation for two vortex core thicknesses corresponding to thin and thick vortex rings. Based on the vortical flow evolution, we may divide the evolution into three typical stages, i.e. approach and slowing, collision and breakdown, and turbulent state. Various fundamental mechanisms dictating the flow behaviors, such as evolution of vortical structures, formation of wrapping vortices, instability of vortex rings, development of modal energies, and transition from laminar to turbulent state, were examined systematically and are summarized briefly as follows.

The evolution of vortical structures is elucidated for the thin or thick vortex ring impacting on a wall. It is noticed that the flow field involves an array of complicated flow phenomena, such as the generation of secondary and tertiary vortex rings, the interaction and deformation of vortex rings, and the instability and breakdown of vortex rings. The evolution of vortical structures is compared for the thin and thick rings. After the secondary vortex ring is generated on the wall, it first evolves around the primary ring,

https://doi.org/10.4208/cicp.150115.210715s Published online by Cambridge University Press

and then moves toward the wall for the thin ring and away from the wall for the thick ring. This behavior is associated with the circulation strength of the secondary ring for the thin and thick ring cases.

The formation of the loop-like and hair-pin vortices wrapping around the vortex rings is investigated. It is found that the hair-pin vortices mostly occur for the thin ring case and the loop-like vortices mostly appear for the thick ring case. The formation of these wrapping vortices is associated with the deformation of vortex rings induced by the strong azimuthal instability. Further, the enstrophy of the wrapping vortices and the TKE are analyzed, indicating that there exists an intrinsic connection of the wrapping vortices with the vortical flow transition to turbulence. On the other hand, the axial flow is investigated because it is related to the vortex ring evolution to turbulent state. It is reasonably obtained that the growth rate of axial flow for the thin ring is faster than that for the thick ring. Moreover, the axial flow should be due to an azimuthal pressure gradient, which is further associated with the growth of azimuthal instability and the core stretching of vortex ring.

The instability of primary and secondary vortex rings and the transition to turbulence are further studied. The perturbation growth relevant to the azimuthal instability is analyzed in the early stage of a vortex ring impinging on a wall. It is learned that the perturbation growth for the secondary ring is faster than that for the primary ring. Further, the Fourier analysis of the vertical vorticity is performed to quantitatively study the characteristics on the azimuthal instabilities of the primary and secondary vortex rings. The dominant modes for the thin and thick vortex rings are determined with the wave number $k=11$ and 6, respectively, consistent with the theoretical estimate $k=2.26/\sigma_0$ [25,]. During the vortical flow evolution, the superharmonic modes are apparent due to the excitation of the unstable mode. As the vortices breaking into small-scale ones, the dominant and superharmonic modes decay rapidly and all the modes exhibit the same order of magnitude. The law of energy decay finally follows a characteristic $k^{-5/3}$ law, indicating that the vortical flow has become turbulent state. Furthermore, it is identified that the TKE is mainly distributed in the core region of vortex rings. The normal stresses are larger than the shear stresses and the azimuthal stress is the dominant component of the normal stresses.

Acknowledgments

This work was supported by the National Natural Science Foundation of China (Grants 11572312, 11372304 and 11132010).

References

[1] K. Shariff and A. Leonard, Vortex rings, Annu. Rev. Fluid Mech., 24 (1992), 235-279.
[2] J. D. A. Walker, C. R. Smith, A. W. Cerra and T. L. Doligalski, The impact of a vortex ring on a wall, J. Fluid Mech., 181 (1987), 99-140.

https://doi.org/10.4208/cicp.150115.210715s Published online by Cambridge University Press

[3] P. Orlandi and R. Verzicco, Vortex rings impinging on walls: axisymmetric and three-dimensional simulations, J. Fluid Mech., 256 (1993), 615-646.
[4] P. J. Archer, T. G. Thomas and G. N. Coleman, The instability of a vortex ring impinging on a free surface, J. Fluid Mech., 642 (2010), 79-94.
[5] U. Boldes and J. C. Ferreri, Behavior of vortex rings in the vicinity of a wall, Phys. Fluids, 16 (1973), 2005-2006.
[6] P. Orlandi, Vortex dipole rebound from a wall, Phys. Fluids A, 2 (1990), 1429-1436.
[7] T. T. Lim, T. B. Nickels and M. S. Chong, A note on the cause of rebound in the head-on collision of a vortex ring with a wall, Exp. Fluids, 12 (1991), 41-48.
[8] C. C. Chu, C. T. Wang and C. S. Hsieh, An experimental investigation of vortex motions near surfaces, Phys. Fluids A, 5 (1993), 662-676.
[9] C. C. Chu, C. T. Wang and C. C. Chang, A vortex ring impinging on a solid plane surface-vortex structure and surface force, Phys. Fluids, 7 (1995), 1391-1401.
[10] D. Fabris, D. Liepmann and D. Marcus, Quantitative experimental and numerical investigation of a vortex ring impinging on a wall, Phys. Fluids, 8 (1996), 2640-2649.
[11] M. Cheng, J. Lou and L. S. Luo, Numerical study of a vortex ring impacting a flat wall, J. Fluid Mech., 660 (2010), 430-455.
[12] L. D. Couch and P. S. Krueger, Experimental investigation of vortex rings impinging on inclined surfaces, Exp. Fluids, 51 (2011), 1123-1138.
[13] C. Krutzsch, Uber eine experimentell beobachtete erscheining an werbelringen bei ehrer translatorischen beivegung in weklechin, flussigheiter, Annln Phys., 5 (1939), 497-523.
[14] S. C. Crow, Stability theory for a pair of trailing vortices, AIAA J., 8 (1970), 2172-2179.
[15] S. E. Widnall, D. B. Bliss and C. Y. Tsai, The instability of short waves on a vortex ring, J. Fluid Mech., 66 (1974), 35-47.
[16] S. E. Widnall and C. Y. Tsai, The instability of the thin vortex ring of constant vorticity, Phil. Trans. R. Soc. Lond. A, 287 (1977), 273-305.
[17] T. Maxworthy, The structure and stability of vortex rings, J. Fluid Mech., 51 (1972), 15-32.
[18] T. Maxworthy, Turbulent vortex rings, J. Fluid Mech., 64 (1974), 227-239.
[19] T. Maxworthy, Some experimental studies of vortex rings, J. Fluid Mech., 81 (1977), 465-495.
[20] S. E. Widnall and J. P. Sullivan, On the stability of vortex rings, Proc. R. Soc. Lond. A, 332 (1973), 335-353.
[21] A. Dazin, P. Dupont and M. Stanislas, Experimental characterization of the instability of the vortex ring. Part I: Linear phase, Exp. Fluids, 40 (2006a), 383-399.
[22] A. Dazin, P. Dupont and M. Stanislas, Experimental characterization of the instability of the vortex ring. Part II: Non-linear phase, Exp. Fluids, 41 (2006b), 401-413.
[23] L. Gan, T. B. Nickels and J. R. Dawson, An experimental study of a turbulent vortex ring: a three-dimensional representation, Exp. Fluids, 51 (2011), 1493-1507.
[24] P. Orlandi and R. Verzicco, Identification of zones in a free evolving vortex ring, Appl. Sci. Res., 53 (1994), 387-399.
[25] K. Shariff, R. Verzicco and P. Orlandi, A numerical study of three-dimensional vortex ring instabilities: viscous corrections and early nonlinear stage, J. Fluid Mech., 279 (1994), 351-375.
[26] M. Bergdorf, P. Koumoutsakos and A. Leonard, Direct numerical simulation of vortex rings at $Re_\Gamma = 7500$, J. Fluid Mech., 581 (2007), 495-505.
[27] P. J. Archer, T. G. Thomas and G. N. Coleman, Direct numerical simulation of vortex ring evolution from the laminar to the early turbulent regime, J. Fluid Mech., 598 (2008), 201-226.
[28] J. D. Swearingen, J. D. Crouch and R. A. Handler, Dynamics and stability of a vortex ring

https://doi.org/10.4208/cicp.150115.210715s Published online by Cambridge University Press

impacting a solid boundary, J. Fluid Mech., 297 (1995), 1-28.
[29] N. Masuda, J. Yoshida, B. Ito, T. Furuya and O. Sana, Collision of a vortex ring on granular material. Part I. Interaction of the vortex ring with the granular layer, Fluid Dyn. Res., 44 (2012), 015501.
[30] J. Yoshida, N. Masuda, B. Ito, T. Furuya and O. Sana, Collision of a vortex ring on granular material. Part II. Erosion of the granular layer, Fluid Dyn. Res., 44 (2012), 015502.
[31] M. Sreedhar and S. Ragab, Large eddy simulation of longitudinal stationary vortices, Phys. Fluids, 6 (1994), 2501-2514.
[32] J. R. Mansfield, O. M. Knio and C. Meneveau, Dynamic LES of colliding vortex rings using a 3D vortex method, J. Comput. Phys., 152 (1999), pp. 305-345.
[33] J. M. Faddy and D. I. Pullin, Flow structure in a model of aircraft trailing vortices, Phys. Fluids, 17 (2005), 085106.
[34] S. Ragab and M. Sreedhar, Numerical simulation of vortices with axial velocity deficits, Phys. Fluids, 7 (1995), 549-558.
[35] X.-Y. Lu, S.-W. Wang, H.-G. Sung, S.-Y. Hsieh and V. Yang, Large-eddy simulations of turbulent swirling flows injected into a dump chamber, J. Fluid Mech., 527 (2005), 171-195.
[36] C.-Y. Xu, L.-W. Chen and X.-Y. Lu, Large eddy simulation of the compressible flow past a wavy cylinder, J. Fluid Mech., 665 (2010), 238-273.
[37] L.-W. Chen, C.-Y. Xu and X.-Y. Lu, Numerical investigation of the compressible flow past an aerofoil, J. Fluid Mech., 643 (2010), 97-126.
[38] L.-W. Chen, G.-L. Wang and X.-Y. Lu, Numerical investigation of a jet from a blunt body opposing a supersonic flow, J. Fluid Mech., 684 (2011), 85-110.
[39] P. G. Saffman, The number of waves on unstable vortex rings, J. Fluid Mech., 84 (1978), 625-639.
[40] S. Krishnamoorthy and J. S. Marshall, Three-dimensional blade-vortex interaction in the strong vortex regime, Phys. Fluids, 10 (1998), 2828-2845.
[41] S. Krishnamoorthy, A. A. Gossler and J. S. Marshall, Normal vortex interaction with a circular cylinder, AAIA J, 37 (1999), 50-57.
[42] A. A. Gossler and J. S. Marshall, Simulation of normal vortex-cylinder interaction in a viscous fluid, J. Fluid Mech., 431 (2001), 371-405.
[43] T. L. Hon and J. D. A. Walker, Evolution of hairpin vortices in a shear flow, Comput. Fluids, 20 (1991), 343-358.
[44] R. J. Adrian, Hairpin vortex organization in wall turbulence, Phys. Fluids, 19 (2007), 041301.
[45] C. Q. Liu and L. Chen, Parallel DNS for vortex structure of late stages of flow transition, Comput. Fluids, 45 (2011), 129-137.
[46] J. Z. Wu, H. Y. Ma and M. D. Zhou, Vorticity and Vortex Dynamics, Springer, 2006.
[47] T. Naitoh, N. Fukuda, T. Gotoh, H. Yamada and K. Nakajima, Experimental study of axial flow in a vortex ring, Phys. Fluids, 14 (2002), 143-149.
[48] F. Laporte and A. Corjon, Direct numerical simulations of the elliptic instability of a vortex pair, Phys. Fluids, 12 (2000), 1016-1031.
[49] P. J. F. de Sousa, Three-dimensional instability on the interaction between a vortex and a stationary sphere, Theor. Comput. Fluid Dyn., 26 (2012), 391-399.
[50] W. M. Rees, F. Hussain and P. Koumoutsakos, Vortex tube reconnection at $Re = 10^4$, Phys. Fluids, 24 (2012), 075105.

https://doi.org/10.4208/cicp.150115.210715s Published online by Cambridge University Press